PAPER

Design of Li$_{1+2x}$Zn$_{1-x}$PS$_4$, a new lithium ion conductor†

William D. Richards,[a] Yan Wang,[a] Lincoln J. Miara,[b] Jae Chul Kim[ac] and Gerbrand Ceder*[acd]

Recent theoretical work has uncovered that a body-centered-cubic (bcc) anion arrangement leads to high ionic conductivity in a number of fast lithium-ion conducting materials. Using this structural feature as a screening criterion, we find that the $I\bar{4}$ material LiZnPS$_4$ contains such a framework and has the potential for very high ionic conductivity. In this work, we apply *ab initio* computational techniques to investigate in detail the ionic conductivity and defect properties of this material. We find that while the stoichiometric structure has poor ionic conductivity, engineering of its composition to introduce interstitial lithium defects is able to exploit the low migration barrier of the bcc anion framework. Our calculations predict a solid-solution regime extending to x = 0.5 in Li$_{1+2x}$Zn$_{1-x}$PS$_4$, and yield a new ionic conductor with exceptionally high lithium-ion conductivity, potentially exceeding 50 mS cm^{-1} at room temperature.

Broader context

Solid-state lithium-ion conductors are promising replacements for the organic liquid electrolytes currently used in many rechargeable batteries. The increasing size of lithium batteries for vehicle and grid applications has made their flammability a real safety concern, which inorganic solid electrolytes could completely address. Currently, the highest-conductivity solid materials are in lithium thiophosphate systems, with Li$_7$P$_3$S$_{11}$ and materials isostructural to Li$_{10}$GeP$_2$S$_{12}$ having conductivities of up to 17 mS cm^{-1} and 25 mS cm^{-1} respectively, even higher than their organic liquid electrolyte counterparts. It has recently been shown that these materials share an underlying bcc anion framework enabling their high conductivity. Using this knowledge to guide the development of a new solid electrolyte, we identify the previously overlooked material LiZnPS$_4$ as also sharing this high-conductivity anion framework. We use first principles calculations to investigate the ionic conductivity, transport mechanisms, and phase stability of this material in detail. We find that introduction of lithium interstitial defects is crucial to high conductivity and fortunately that a large Li-interstitial defect concentration is possible in Li$_{1+2x}$Zn$_{1-x}$PS$_4$, potentially allowing it to exceed the conductivity of current state-of-the-art electrolytes. This material also provides further evidence of the importance of the anion framework in high conductivity materials.

Research into solid inorganic lithium-ion conductors has exploded in recent years due to their position as the most promising alternative to the flammable organic solvent electrolytes currently used in intercalation batteries. In addition to being thermally stable and highly resistant to oxidation, inorganic electrolyte materials have the potential to significantly improve battery performance by improving packing efficiency and cycle life with high voltage cathodes.[1] Many of the highest conductivity materials are in the lithium thiophosphate system, including the glass-ceramic material Li$_7$P$_3$S$_{11}$ which achieves a room temperature (RT) conductivity of 17 mS cm^{-1},[2] Li$_{10}$GeP$_2$S$_{12}$ (LGPS) with a RT conductivity of 12 mS cm^{-1},[3] and recently optimized materials isostructural to LGPS having RT conductivity as high as 25 mS cm^{-1},[4–7] consistent with our previously made predictions.[8] Remarkably, the conductivity of these thiophosphate materials even surpasses that of the liquid electrolyte LiPF$_6$ in EC/DMC, the electrolyte most commonly used in commercial cells today.[9] Recent theoretical work has revealed that these highest-performing thiophosphate materials share a body-centered-cubic (bcc) sulfur anion arrangement that permits high ionic conductivity due to its interconnected network of energetically equivalent tetrahedral sites.[10] We use this insight to design a new lithium-ion conductor based on LiZnPS$_4$ (LZPS),[11] finding a solid-solution

a Department of Materials Science and Engineering, Massachusetts Institute of Technology, 77 Massachusetts Ave., Cambridge, MA 02139, USA

b Samsung Advanced Institute of Technology – USA, 255 Main St., Suite 702, Cambridge, MA 02142, USA

c Materials Sciences Division, Lawrence Berkeley National Laboratory, Berkeley, CA 94720, USA

d Department of Materials Science and Engineering, University of California, Berkeley, CA 94720, USA. E-mail: gceder@berkeley.edu

† Electronic supplementary information (ESI) available: S^{2-} substructure matching visualization. Phonon densities of states. See DOI: 10.1039/c6ee02094a

3272 | *Energy Environ. Sci.*, 2016, **9**, 3272–3278

This journal is © The Royal Society of Chemistry 2016

regime extending to $x = 0.5$ in $Li_{1+2x}Zn_{1-x}PS_4$ and the potential to surpass the high conductivities of existing lithium thiophosphate materials.

Structural screening of materials in the Inorganic Crystal Structure Database (ICSD)[12] reveals that the crystal structure of LZPS contains a bcc arrangement of sulfur anions and may therefore be expected to have high lithium-ion mobility. The crystal structure of LZPS has previously been characterized,[11] but to the best of our knowledge it has never been studied in the context of ionic conduction. In this work, we apply computational techniques based on density functional theory (DFT) to evaluate the stability of LZPS and the mechanism of ionic transport in this material. We apply *ab initio* molecular dynamics (AIMD) simulations to probe its conductivity, and nudged elastic band simulations to investigate the transport mechanisms in greater detail. These techniques have had great success in replicating experimentally measured conductivity of some of the highest performing thiophosphate conductors including $Li_{10}GeP_2S_{12}$[3,13] and $Li_7P_3S_{11}$,[2,14] and more importantly in accurately predicting existence of new materials and their conductivities before their experimental realization, including the Sn and Si versions of LGPS and their Na analogs.[5–8,15] To investigate the defect solubility and therefore the feasibility of experimentally obtaining off-stoichiometric compositions in this structure, we compute the finite-temperature phase diagram using cluster expansion Monte Carlo and frozen phonon calculations to capture the effects of configurational and vibrational entropy respectively.

1 Methods and results

1.1 Crystal structure

The crystal structure of $LiZnPS_4$ (Fig. 1a) can be described as two alternating layers of corner sharing sulfur tetrahedra perpendicular to the *c*-axis. In the stoichiometric structure, one layer is half occupied by phosphorus (P layer) and the other contains an ordered arrangement of Li and Zn atoms (Zn layer). Using an
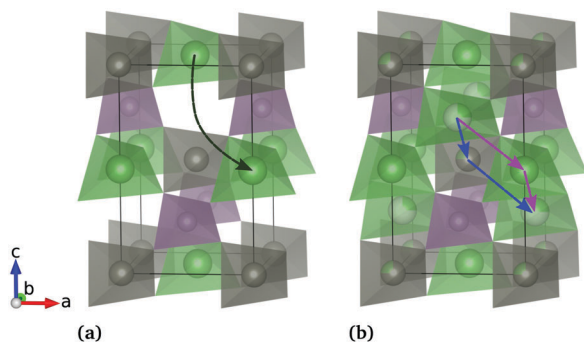

Fig. 1 Structures of (a) ordered $LiZnPS_4$, and (b) off-stoichiometric disordered $Li_{1+2x}Zn_{1-x}PS_4$. Purple PS_4, grey ZnS_4, and green LiS_4 tetrahedra. When the Li concentration is increased, Li^+-ions begin to occupy vacant tetrahedral sites in the P layer, compensated by substitution of a Li^+ for a nearby Zn^{2+}. The primary transport mechanisms of each structure are shown schematically with an arrow indicating the atom motion. Each color represents a separate mechanism.

affine-mapping transformation as implemented in the pymatgen software package[16] we match the sulfur sublattice to a body centered tetragonal (bct) framework. This affine mapping transforms the LZPS lattice exactly onto lattice points belonging to the bct lattice, while minimizing the root-mean-square distance between the atom positions in the two lattices. We find that the S^{2-} sublattice in LZPS is very close to bcc, having an a/c ratio of 0.9 and with sulfur atoms each displaced only 0.29 Å from their ideal positions (Fig. S1, ESI†). This compares favorably with the crystal structure of other known lithium superionic conductors.[10]

In addition to the stoichiometric structure, we are interested in studying the conduction properties of the Li-rich compositions of $Li_{1+2x}Zn_{1-x}PS_4$ with $x > 0$. As excess lithium is introduced, we expect lithium ions to occupy vacant sites in the P layer (which we will refer to as Li^+-interstitials) since there are no remaining non-edge-sharing sites available in the Zn layer (Fig. 1b). This is confirmed by DFT calculations of the alternative interstitial configurations; Li-ions initialized in the edge sharing tetrahedral site in the Zn-layer and in the octahedral site between the Zn and P layers both relax to the corner-sharing tetrahedral site in the P layer. Preferred Li-occupancy of the P layer is also shown by the Li-ion probability density calculated from AIMD simulations (Fig. S2, ESI†). Because of the relatively small size of the PS_4 tetrahedron, the P layer is slightly thinner than the Zn layer and these remaining tetrahedral sites are high energy in comparison to the standard Li_{Li}-sites. Each interstitial Li^+ is charge compensated by substitution of a nearby Zn^{2+} atom with Li^+. Our calculations will show that this occupancy is crucial for improving ionic transport.

1.2 Ionic conductivity

The bcc anion sublattice of LZPS suggests that it will have high lithium ion mobility, which we confirm using *ab initio* molecular dynamics simulations (AIMD), and nudged elastic band (NEB) calculations, both using DFT to calculate energies and forces. The presence of defects can have very significant effects on ionic transport; we calculate the diffusivity and ionic conductivity of the pristine structure and at a range of defect concentrations on $Li_{1+2x}Zn_{1-x}PS_4$, from $x = 0$ to $x = 0.75$. This compositional range was selected for the expected high mobility and low defect energy of this interstitial defect. All DFT calculations are use the Perdew–Burke–Ernzerhof (PBE) generalized gradient approximations[17] using the projector augmented wave (PAW) method[18] as implemented in the Vienna *Ab initio* Simulation Package (VASP).[19] Pseudopotentials used were PAW_PBE Zn 06Sep2000, PAW_PBE Li 17Jan2003, PAW_PBE P 17Jan2003, and PAW_PBE S 17Jan2003. For AIMD and NEB calculations, the energy cutoff was 280 eV.

1.2.1 *Ab initio* molecular dynamics. AIMD determines the Li-ion diffusivity by simulating atomic motion at elevated temperatures and calculating from atom trajectories the diffusivity (D_{Li}) through the Einstein relation (eqn (1), where d is the dimensionality of the system, t the elapsed time, and $\langle \|\Delta \mathbf{x}\|^2 \rangle$ the mean squared atom displacement). Ionic conductivity is obtained from the diffusivity using the Nernst–Einstein relation

This journal is © The Royal Society of Chemistry 2016

Energy Environ. Sci., 2016, **9**, 3272–3278 | 3273

(eqn (2), where $z_{Li}e$ the charge on a Li^+ ion, c_{Li} is the concentration of Li ions, T the temperature, and k_B Boltzmann's constant).

$$\langle \|\Delta \mathbf{x}\|^2 \rangle = 2dD_{Li}t \qquad (1)$$

$$\sigma_{Li} = \frac{(z_{Li}e)^2 c_{Li} D_{Li}}{k_B T} \qquad (2)$$

For these AIMD calculations, an *NVT* ensemble was simulated using a time step of 2 fs and a Nosé–Hoover thermostat[20] with a period of 80 fs. A minimal Γ-point only k-point grid was used, and calculations were non-spin-polarized. The lowest energy atomic arrangement on a $2 \times 2 \times 1$ supercell of the conventional cell (Fig. 1) was simulated for each composition. AIMD simulations were run every 100 K between 400 and 900 K for 240 000 time steps (480 ps). Results of the simulations are shown in Fig. 2, and calculated diffusivities, activation energies, and extrapolated room temperature conductivities in Table 1. For the stoichiometric structure $LiZnPS_4$, diffusion calculations below 700 K did not converge due to the low amount of atomic motion in the simulations.

The AIMD simulations show a very strong trend of increasing conductivity with lithium-ion concentration, with extrapolated room temperature conductivity increasing by ten orders of magnitude between the $x = 0$ and $x = 0.75$ compositions. The maximum RT conductivity obtained, 114 mS cm^{-1} at $Li_{2.5}Zn_{0.25}PS_4$ is significantly higher than that of any known solid Li-ion conductor. While the stoichiometric compound has a very high activation energy, reflecting the need to thermally create carriers, as soon as Li-excess is introduced the activation energy drops to the low values expected for the bcc anion framework. The mechanisms of this diffusion process and the feasibility of attaining these compositions, will be investigated in the next sections.

1.2.2 Nudged elastic band calculations. To better understand the transport mechanisms in this material, we performed nudged elastic band (NEB)[21] calculations of the vacancy migration barrier and cooperative migration in $Li_{10}Zn_7P_8S_{32}$, along

Table 1 Calculated activation energy (E_a) and extrapolated room temperature (RT) conductivity for $Li_{1+2x}Zn_{1-x}PS_4$ from MD simulations

Composition	E_a/eV	RT conductivity/mS cm^{-1}
$LiZnPS_4$	1.07	1.81×10^{-9}
$Li_{1.25}Zn_{0.875}PS_4$	0.252	3.44
$Li_{1.5}Zn_{0.75}PS_4$	0.181	27.7
$Li_2Zn_{0.5}PS_4$	0.165	53.8
$Li_{2.5}Zn_{0.25}PS_4$	0.140	114

the ion paths shown schematically in Fig. 1. NEB calculations determine the migration energy required to reach the transition state, which is closely related to the activation energy for transport in the Arrhenius relation of the ionic conductivity.

We distinguish three mechanisms: the vacancy migration mechanism (Fig. 1a) tracks the motion of a Li-vacancy from one Zn layer to another, with a Li-ion passing through the empty tetrahedral site in the phosphorus layer; in Li^+-interstitial migration, there are two relevant cooperative mechanisms (Fig. 1b) that result in net motion of one Li^+-interstitial moving between P layers. Because of the difference in Li-site energy between the P and Zn layers, lithium vacancies in the Zn layer are unstable and migration must start and end with full occupancy of the Zn layer. In both cooperative pathways, an interstitial Li-ion moves from the P to Zn layer, displacing a second Li-ion that moves to a vacant site in the P layer. Under Li-excess, some of the zinc atoms in the stoichiometric structure are replaced by lithium, so this cooperative mechanism can occur either through a Li_{Li}-site (purple arrow), or through a Li_{Zn}-site (blue arrow). These sites are structurally very similar, but differ in the occupancy of their in-layer tetrahedral neighbors: Zn for the Li_{Li}-site, Li for the Li_{Zn} site. Whereas the vacancy migration and cooperative path through the Li_{Li}-site are inherently percolating 3d conduction pathways, percolation of the Li_{Zn} pathway requires a high lithium content to increase the number of these sites.

For the vacancy mechanism NEB calculation, the defect charge is compensated by a uniform background charge to retain the oxidation states of the pristine structure. The calculations for the cooperative mechanisms use a structure with the composition $Li_{1.25}Zn_{0.875}PS_4$. The calculated energies of these three pathways are shown in Fig. 3.

The vacancy migration barrier is calculated to be 414 meV, much higher than that of interstitial lithium through the Li_{Zn} site, 226 meV, and the interstitial path through the Li_{Li} site calculated to be 358 meV. At room temperature the difference between the high and low barriers corresponds approximately to three orders of magnitude in lithium diffusivity, emphasizing the importance of achieving interstitial rather than vacancy defects for conductivity.

The vacancy migration barrier (414 meV) is, however, still much lower than the activation energy calculated from AIMD in stoichiometric $LiZnPS_4$ (1070 meV). This is to be expected as there are no extrinsic defects at the stoichiometric composition and their formation energy will contribute significantly to the measured activation energy. The large increase in the AIMD calculated conductivity with increasing lithium concentration
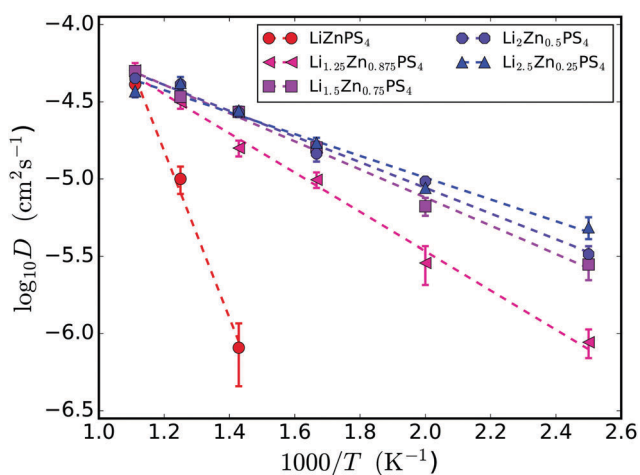

Fig. 2 Arrhenius plot of Li-ion diffusivity in $Li_{1+2x}Zn_{1-x}PS_4$ from AIMD simulations. Dotted lines are least-squares fits to the data.
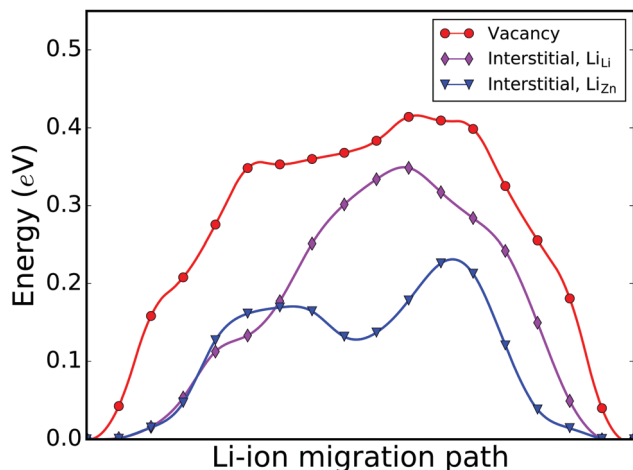
Fig. 3 Energy along the minimal energy pathway for a charge-compensated vacancy defect (red) and an interstitial with cooperative motion (blue, through Li_{Zn}, and purple, through Li_{Li}) in $Li_{1.25}Zn_{0.875}PS_4$.

(Table 1) is due to a combination of (1) the introduction of extrinsic defects, (2) the lower energy barrier of the cooperative Li migration, and (3) an increase in the number of Li_{Zn} sites, allowing percolation by this lower energy mechanism. It is clear that LZPS can achieve a very high conductivity if high enough off-stoichiometry can be achieved. In the next section we use *ab initio* phase diagram methods to investigate the solubility limits in LZPS.

1.3 Defect solubility

1.3.1 Cluster expansion. Because of the high conductivity of the interstitial defect in $Li_{1+2x}Zn_{1-x}PS_4$, it is particularly important to understand its solubility limit. We calculate the finite-temperature pseudo-binary phase diagram between the $I\bar{4}$ $LiZnPS_4$ and the $Pmn2_1$ phase of γ-Li_3PS_4,[22] the ground state structure at the Li_3PS_4 composition, to determine the accessible compositional range of this solid solution. Two high temperature polymorphs of Li_3PS_4, β and α, are also observed in this system,[22] but the DFT enthalpy and phonon free energies predict a transition from the γ to β-phase above 850 K, and so inclusion of these polymorphs would have a minimal effect on the calculated defect solubility of $Li_{1+2x}Zn_{1-x}PS_4$ over the considered temperature range of 0 to 1000 K. We confirm that the pseudo-binary equilibrium is the relevant decomposition along this tieline (*i.e.* that no other phases, or lower energy equilibrium of other phases, exists in the quaternary phase diagram between these end members) by calculating the energies of all known compounds in the Li–Zn–P–S chemical space and those generated by applying a data-mined ionic substitution algorithm[23] to known crystal structures in other chemical systems using a probability threshold of 10^{-4}. From these energies, we construct the ground state (0 K) phase diagram (Fig. S3, ESI†) using the convex hull implementation of the pymatgen software package.[16] This methodology finds all compositions that cannot lower their energy by decomposing into any combination of other phases. From these calculations, we find that the end members, $LiZnPS_4$ and γ-Li_3PS_4, are

indeed stable, and that compositions between these phases decompose to a mixture of these end members at 0 K.

Cluster expansions represent the energy of a periodic arrangement of atoms as a function of their local environments, and are a well-established techniques for calculating configurational entropy for phase diagrams.[24–29] Total energy calculations for the phase diagram and for fitting the cluster expansion use an energy cutoff of 520 eV, a *k*-point grid containing at least 1000/n_{atoms}, and are spin-polarized for compatibility with previous total energy calculations and phase diagrams.[30] For both the γ-Li_3PS_4 and $Li_{1+2x}Zn_{1-x}PS_4$ structures we build an energy model consisting of a short range cluster expansion containing point terms, pair terms to 8 Å, and triplet terms to 5 Å, and a long range electrostatic component modeling the interactions between ideal charges on each ion (*i.e.* Li^+, Zn^{2+}, P^{5+}, S^{2-}) parameterized by the relative permittivity. The cluster expansion and long range electrostatic interactions are fit simultaneously to ensure that the electrostatic model captures only the long range effects.

The $I\bar{4}$ structure requires a coupled-cluster expansion[31] with a lattice of Li/vacancy and another of Li/Zn occupancy, and the $Pmn2_1$ structure a ternary cluster expansion with Li/Zn/vacancy occupancy on two distinct sites. This model is fit to DFT computed structures using a compressive sensing approach[32–34] penalizing the L_1-norm of the effective cluster interactions (ECI's, u) according to eqn (3), in which A is the feature matrix and f the DFT computed structure energies, using the split-Bregman algorithm.[33] The error term weight (μ) was chosen for each lattice to minimize the out-of-sample root mean square error.

$$\mathbf{u} = \underset{\mathbf{u}}{\mathrm{argmin}}\left\{\parallel \mathbf{u} \parallel_1 + \frac{\mu}{2}\parallel A\mathbf{u} - \mathbf{f}\parallel_2^2\right\} \quad (3)$$

The out-of-sample root mean square error of these cluster expansions, as calculated from 5-fold cross validation, was 3.1 meV per formula unit (1.6 meV p.f.u. in-sample error; 2 Li/Zn sites and one Li/vacancy site) for the $I\bar{4}$ lattice, and 3.5 meV p.f.u. (2.1 meV p.f.u. in-sample error; 3 sites with Li/Zn/vacancy occupancy) for the $Pmn2_1$ lattice. These errors are small on the energy scale of the disordering transformation ($\sim$75 meV p.f.u.). We calculate the internal energy as a function of temperature for each of these phases from canonical ensemble (constant composition) Monte Carlo simulations using the Metropolis–Hastings algorithm[35] at 33 evenly-spaced compositions between $LiZnPS_4$ and Li_3PS_4. In these calculations, each Monte Carlo cell contains 64 formula units and has lattice vectors of at least 20 Å. Ten million Monte Carlo perturbations (MC steps) were simulated at each temperature after an initial equilibration period of one million MC steps. Twenty temperatures between 0 K and 1200 K were simulated at each composition, with internal energies at intermediate values computed by reweighting the observed energies from nearby temperatures.[36] Entropies and free energies are obtained from these calculation by thermodynamic integration at each composition from 0 K according to eqn (4), where C_p is the heat capacity, k_B Boltzmann's constant, and Ω_{gs} the degeneracy of the ground state structure.

$$S = k_B \log(\Omega_{gs}) + \int_0^T \frac{C_p}{T} dT \quad (4)$$

This journal is © The Royal Society of Chemistry 2016

Energy Environ. Sci., 2016, **9**, 3272–3278 | **3275**

The degeneracy of the ground state is included here because we have confined the system to a specific periodicity and composition, and therefore the ground state entropy of this system is not defined to be 0 at 0 K.

1.3.2 Phonon calculations. The effects of phonons are calculated using the phonopy software package.[37] Because of the large computational expense of these calculations, especially for low symmetry structures, phonon free energy calculations were calculated for $x = 0$, 0.5, and 1 compositions within each lattice, and values for intermediate compositions were interpolated from these calculations. At each of these compositions, the lowest energy configuration on the orthorhombic conventional cell containing 2 formula units was used. The phonon calculation calculated the Hessian matrix for orthorhombic supercells with lattice vectors as close as possible to 20 Å.

The results of the phonon calculations, shown in Table 2, show a stabilizing effect on the high-conductivity $I\bar{4}$ structures. To display the effects on relative phase stability more easily, we have referenced all thermodynamic values to those of the $I\bar{4}$ phase at LiZnPS$_4$ and of the $Pmn2_1$ phase at Li$_3$PS$_4$. While the magnitude of the effect of the phonons is roughly similar to that of the configurational entropy, the phonons have a much greater effect on phase selection in the off-stoichiometric structures – a difference of almost 30 meV p.f.u. in phonon free energy between phases at 600 K, compared to a difference of 7.5 meV p.f.u. for the configurational entropy. From the projected phonon densities of states (shown in Fig. S4, ESI†), this stabilization is seen to be a result of the lower phonon frequency of the lithium in the phosphorus layers relative to the non-defect Li, which is consistent with the low activation energy of the cooperative defect mechanism.

1.3.3 Finite temperature phase diagram. We combine the results of the phonon and cluster expansion Monte Carlo calculations to produce the pseudo-binary phase diagram in Fig. 4. For calculation of the phase diagram, configurational free energies are smoothed across compositional space to eliminate artifacts from the finite cell size of the Monte Carlo calculations, and the behavior at the extremes of composition (*i.e.* in the very low-defect limits) is fit to a regular solution
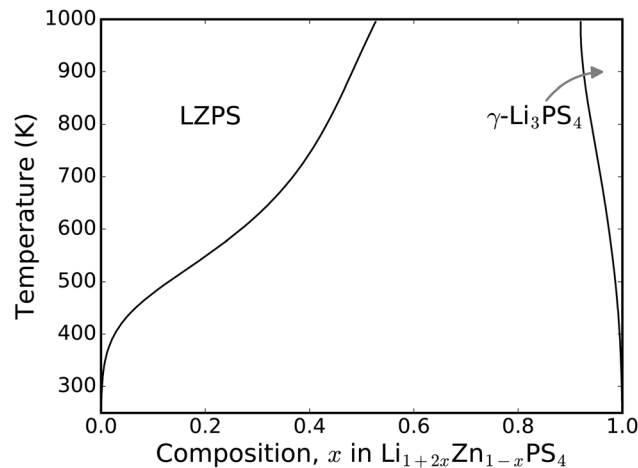

Fig. 4 Pseudo-binary phase diagram of the LiZnPS$_4$–γ-Li$_3$PS$_4$ system, generated from cluster expansion Monte Carlo and phonon calculations.

model to ensure physically reasonable solubilities at these extrema. The free energies from phonon calculations were added to these configurational free energies, and the solubility limits found by the intersection of the common tangent with the free energy curves at each temperature. The calculated phase diagram shows that the Li$_2$Zn$_{0.5}$PS$_4$ ($x = 0.5$) composition is stabilized above $\sim$950 K. Emphasizing the importance of the phonon free energy on the defect solubility, the phase diagram calculated without phonons shows a maximum solubility of only $x = 0.15$ (Fig. S5, ESI†).

2 Discussion

LZPS can be added to the short but growing list of ionic conductors with a bcc anion framework and exceptionally high mobility. Computational analysis of this material demonstrates that the bcc structural framework guarantees that there is a low barrier between the interconnected tetrahedral sites only if the sites themselves have similar energies; the introduction of interstitial Li-ion defects is key to unlocking the high performance of LZPS due to the different character of the Li/Zn and P layers. Analysis of this material *via* the kinetically resolved activation barrier technique[38] (*i.e.* by comparing the energy of the transition state to the average of the endpoint energies) yields a barrier of $\sim$150 meV, which would yield exceptionally fast diffusion, and is very much in line with the estimate for the idealized sulfur lattice in ref. 10. Adding an interstitial defect causes at least one Li atom to be in the higher energy state at all times and smooths out the energy landscape considerably, evidenced by the lower activation energies both in the NEB (Fig. 3) and MD calculations (Table 1 and Fig. 2).

The extremely high solubility of the Li-interstitial defect in the LZPS structure is aided by the coupling between the Zn layer and the Li-interstitials. At low temperatures, order on the Zn layer makes the insertion of Li-interstitials energetically unfavorable. At moderate temperatures, above around 400 K

Table 2 0 K enthalpy and free energy contributions from phonons and configurational entropy for the $I\bar{4}$ and $Pmn2_1$ phases at 600 K. All values have been referenced to the $I\bar{4}$ phase at LiZnPS$_4$ and the $Pmn2_1$ phase at Li$_3$PS$_4$

	Composition		
	LiZnPS$_4$	Li$_2$Zn$_{0.5}$PS$_4$	Li$_3$PS$_4$
0 K enthalpy (meV f.u.$^{-1}$)			
$I\bar{4}$	0	77.1	90.2
$Pmn2_1$	n/a	73.0	0
Configurational free energy (meV f.u.$^{-1}$)			
$I\bar{4}$	0	−35.2	0
$Pmn2_1$	n/a	−28.7	0
Phonon free energy (meV f.u.$^{-1}$)			
$I\bar{4}$	0	−42.7	9.8
$Pmn2_1$	n/a	−13.9	0

3276 | *Energy Environ. Sci.*, 2016, **9**, 3272–3278

This journal is © The Royal Society of Chemistry 2016

across the compositional range, adding lithium interstitials and replacing some Zn with Li allows this layer to disorder more easily, increasing the entropic driving force for interstitial incorporation.

Many thiophosphate conductor materials, in particular those containing metal or metalloid elements, are not stable against pure lithium.[5,8,13,39] Contact with a lithium metal anode may reduce the Zn^{2+} in LZPS and result in electrical conductivity similar to $Li_{10}GeP_2S_{12}$ and related materials. However, $Li_{9.54}Si_{1.74}P_{1.44}S_{11.7}Cl_{0.3}$ has been shown to be effective in combination with a $Li_4Ti_5O_{12}$ anode in a high-rate cell.[4] The more negative formation energy per sulfur atom of ZnS compared to SiS_2[40] suggests that the low voltage stability limit of Zn-containing sulfides will be ~ 0.5 V lower than Si-containing sulfides. Interfacial stability with low voltage anodes may alternately be achieved with the use of an electronically insulating anode coating.

LZPS also illustrates the importance of phonon stabilization in ionic conductors. The two competing lattices, based on the $LiZnPS_4$ and γ-Li_3PS_4 structures, have similar configurational entropy and enthalpy for the $Li_2Zn_{0.5}PS_4$ composition (Table 2), but the excess phonon free energy is much higher for the LZPS structure with its highly mobile Li sublattice. Our calculations show the typical phenomenon of the effects of phonon free energies being similar in magnitude to those of configurational entropy.[41,42] The importance of phonons in stabilizing ionically conducting materials has been noted previously in similar materials including $Na_{10}GeP_2S_{12}$[15,43] and $Li_7P_3S_{11}$,[14] but here it is especially apparent also in its stark effect on defect solubility.

The calculated migration barriers (Fig. 3) are significantly lower for the Li interstitial through the Li_{Zn} site, compared to the Li_{Li} site. It is therefore desirable to increase the number of such sites to achieve percolation through the low energy pathway. This can be done by increasing the Li content through the $Zn^{2+} \rightarrow 2Li^+$ substitution, as has been investigated in this paper. An alternative method may be to replace some Zn with Li and charge compensate that substitution with doping on the anion lattice (e.g. $S^{2-} \rightarrow Cl^-$) or doping on the Zn site (e.g. $Zn^{2+} \rightarrow Ga^{3+}$). This would reduce the number of (high energy) lithium interstitials required for the low activation energy pathway to become percolating, and so higher Li_{Zn} concentrations may be achievable by these means.

3 Conclusions

We have applied the recently discovered design criterion of a bcc anion sublattice together with *ab initio* computational methods to predict a new lithium thiophosphate conductor with a large range of solubility, $Li_{1+2x}Zn_{1-x}PS_4$ ($0 \leq x < 0.5$), and extraordinarily high conductivity. We show that the highly defective compositions on this framework have the potential for the greatest room temperature conductivity of any solid lithium ion conductor, and that the maximum conductivity is limited by the defect solubility. If the solubility range could somehow be extended further to $Li_{2.5}Zn_{0.25}PS_4$ ($x = 0.75$), a

conductivity in excess of 100 mS cm^{-1} may be attainable. Even with the $x < 0.5$ limitation, the high defect solubility yields an expected ionic conductivity of 54 mS cm^{-1}, exceeding the performance of current state-of-the-art. The combination of molecular dynamics studies across a range of compositions and detailed mechanical analysis of lithium ion transport leads to an in-depth understanding of the factors governing ionic diffusion in this new class of materials, as well as identifying pathways to further improve conductivity.

Acknowledgements

References

1 J. Li, C. Ma, M. Chi, C. Liang and N. J. Dudney, *Adv. Energy Mater.*, 2015, **5**, 1401408.

2 Y. Seino, T. Ota, K. Takada, A. Hayashi and M. Tatsumisago, *Energy Environ. Sci.*, 2014, **7**, 627–631.

3 N. Kamaya, K. Homma, Y. Yamakawa, M. Hirayama, R. Kanno, M. Yonemura, T. Kamiyama, Y. Kato, S. Hama, K. Kawamoto and A. Mitsui, *Nat. Mater.*, 2011, **10**, 682–686.

4 Y. Kato, S. Hori, T. Saito, K. Suzuki, M. Hirayama, A. Mitsui, M. Yonemura, H. Iba and R. Kanno, *Nat. Energy*, 2016, **1**, 16030.

5 J. M. Whiteley, J. H. Woo, E. Hu, K.-W. Nam and S.-H. Lee, *J. Electrochem. Soc.*, 2014, **161**, A1812–A1817.

6 A. Kuhn, O. Gerbig, C. Zhu, F. Falkenberg, J. Maier and B. V. Lotsch, *Phys. Chem. Chem. Phys.*, 2014, **16**, 14669–14674.

7 P. Bron, S. Johansson, K. Zick, J. Schmedt auf der Günne, S. Dehnen and B. Roling, *J. Am. Chem. Soc.*, 2013, **135**, 15694–15697.

8 S. P. Ong, Y. Mo, W. D. Richards, L. Miara, H. S. Lee and G. Ceder, *Energy Environ. Sci.*, 2013, **6**, 148–156.

9 L. O. Valøen and J. N. Reimers, *J. Electrochem. Soc.*, 2005, **152**, A882.

10 Y. Wang, W. D. Richards, S. P. Ong, L. J. Miara, J. C. Kim, Y. Mo and G. Ceder, *Nat. Mater.*, 2015, **14**, 1026–1031.

11 S. Jörgens, D. Johrendt and A. Mewis, *Z. Anorg. Allg. Chem.*, 2002, **628**, 1765.

12 A. Belsky, M. Hellenbrandt, V. L. Karen and P. Luksch, *Acta Crystallogr., Sect. B: Struct. Sci.*, 2002, **58**, 364–369.

13 Y. Mo, S. P. Ong and G. Ceder, *Chem. Mater.*, 2012, **24**, 15–17.

14 I.-H. Chu, H. Nguyen, S. Hy, Y.-C. Lin, Z. Wang, Z. Xu, Z. Deng, Y. S. Meng and S. P. Ong, *ACS Appl. Mater. Interfaces*, 2016, **8**, 7843–7853.

15 W. D. Richards, T. Tsujimura, L. J. Miara, Y. Wang, J. C. Kim, S. P. Ong, I. Uechi, N. Suzuki and G. Ceder, *Nat. Commun.*, 2016, **7**, 11009.

This journal is © The Royal Society of Chemistry 2016

Energy Environ. Sci., 2016, **9**, 3272–3278 | 3277

16 S. P. Ong, W. D. Richards, A. Jain, G. Hautier, M. Kocher, S. Cholia, D. Gunter, V. L. Chevrier, K. A. Persson and G. Ceder, *Comput. Mater. Sci.*, 2013, **68**, 314–319.

17 J. P. Perdew, K. Burke and M. Ernzerhof, *Phys. Rev. Lett.*, 1996, **77**, 3865–3868.

18 P. E. Blöchl, *Phys. Rev. B: Condens. Matter Mater. Phys.*, 1994, **50**, 17953–17979.

19 G. Kresse and J. Furthmüller, *Phys. Rev. B: Condens. Matter Mater. Phys.*, 1996, **54**, 11169–11186.

20 S. Nosé, *J. Chem. Phys.*, 1984, **81**, 511–519.

21 H. Jonsson, G. Mills and K. Jacobsen, *Class. quantum dyn. condens. phase simulations*, World Scientific, 1998, pp. 385–404.

22 K. Homma, M. Yonemura, T. Kobayashi, M. Nagao, M. Hirayama and R. Kanno, *Solid State Ionics*, 2011, **182**, 53–58.

23 G. Hautier, C. Fischer, V. Ehrlacher, A. Jain and G. Ceder, *Inorg. Chem.*, 2011, **50**, 656–663.

24 J. M. Sanchez, J. P. Stark and V. L. Moruzzi, *Phys. Rev. B: Condens. Matter Mater. Phys.*, 1991, **44**, 5411–5418.

25 J. Sanchez, F. Ducastelle and D. Gratias, *Phys. A*, 1984, **128**, 334–350.

26 D. D. Fontaine, *Solid State Phys. – Adv. Res. Appl.*, Academic Press, Inc., 1994, vol. 47, pp. 33–176.

27 G. Ceder, P. D. Tepesch, A. F. Kohan and A. Van der Ven, *J. Electroceram.*, 1997, **1**, 15–26.

28 V. Ozolins, C. Wolverton and A. Zunger, *Phys. Rev. B: Condens. Matter Mater. Phys.*, 1998, **57**, 6427–6443.

29 A. van de Walle and G. Ceder, *J. Phase Equilib.*, 2002, **23**, 348–359.

30 A. Jain, G. Hautier, C. J. Moore, S. P. Ong, C. C. Fischer, T. Mueller, K. A. Persson and G. Ceder, *Comput. Mater. Sci.*, 2011, **50**, 2295–2310.

31 P. D. Tepesch, G. D. Garbulsky and G. Ceder, *Phys. Rev. Lett.*, 1995, **74**, 2272–2275.

32 E. Candes and M. Wakin, *IEEE Signal Process. Mag.*, 2008, **25**, 21–30.

33 T. Goldstein and S. Osher, *SIAM J. Imaging Sci.*, 2009, **2**, 323–343.

34 L. J. Nelson, G. L. W. Hart, F. Zhou and V. Ozolins, *Phys. Rev. B: Condens. Matter Mater. Phys.*, 2013, **87**, 035125.

35 W. K. Hastings, *Biometrika*, 1970, **57**, 97–109.

36 A. M. Ferrenberg and R. H. Swendsen, *Phys. Rev. Lett.*, 1988, **61**, 2635–2638.

37 A. Togo and I. Tanaka, *Scr. Mater.*, 2015, **108**, 1–5.

38 A. Van der Ven, G. Ceder, M. Asta and P. D. Tepesch, *Phys. Rev. B: Condens. Matter Mater. Phys.*, 2001, **64**, 184307.

39 W. D. Richards, L. J. Miara, Y. Wang, J. C. Kim and G. Ceder, *Chem. Mater.*, 2016, **28**, 266–273.

40 O. Kubaschewski, C. B. Alcock and P. J. Spencer, *Materials Thermochemistry*, Pergamon Press, Oxford, 6th edn, 1993.

41 L. Anthony, L. J. Nagel, J. K. Okamoto and B. Fultz, *Phys. Rev. Lett.*, 1994, **73**, 3034–3037.

42 A. van de Walle, G. Ceder and U. V. Waghmare, *Phys. Rev. Lett.*, 1998, **80**, 4911–4914.

43 V. S. Kandagal, M. D. Bharadwaj and U. V. Waghmare, *J. Mater. Chem. A*, 2015, **3**, 12992–12999.

3278 | *Energy Environ. Sci.*, 2016, **9**, 3272–3278

This journal is © The Royal Society of Chemistry 2016